INTERNATIONAL JOURNAL OF NUMERICAL MODELLING: ELECTRONIC NETWORKS, DEVICES AND FIELDS
Int. J. Numer. Model. (2012)
Published online in Wiley Online Library (wileyonlinelibrary.com). DOI: 10.1002/jnm.1875

openEMS – a free and open source equivalent-circuit (EC) FDTD simulation platform supporting cylindrical coordinates suitable for the analysis of traveling wave MRI applications

Thorsten Liebig*,†, Andreas Rennings, Sebastian Held and Daniel Erni

General and Theoretical Electrical Engineering (ATE), Faculty of Engineering, University of Duisburg-Essen, and CENIDE - Center for Nanointegration Duisburg-Essen, D-47057 Duisburg, Germany

SUMMARY

In this paper, we present a free and open source platform by using the equivalent-circuit finite-difference time-domain (FDTD) method adapted to cylindrical coordinates to efficiently model cylindrically shaped objects. We will address the special characteristics of a cylindrical FDTD mesh such as the mesh singularity at $r = 0$ and discuss how cylindrical subgrids for small radii can reduce the simulation time considerably. Furthermore, we will demonstrate the applicability and advantages of this cylindrical equivalent-circuit FDTD method to evaluate new types of conformal ring antennas used in the context of high-field (7T) traveling wave magnetic resonance imaging (MRI). Copyright © 2012 John Wiley & Sons, Ltd.

Received 2 March 2012; Revised 10 July 2012; Accepted 3 October 2012

KEY WORDS: FDTD; EC FDTD; cylindrical mesh; multigrid; traveling wave MRI

1. INTRODUCTION

The finite-difference time-domain (FDTD) method is one of the most successful explicit and direct numerical methods to solve large and complex electromagnetic field problems [1,2]. Its greatest benefit is the simple and straightforward approach allowing a memory and computationally efficient implementation. The conventional field-based version of the FDTD method [1, 2] relies on both the electric and magnetic field components involving the typical leapfrogged multiply-and-add updating scheme for the well-known time evolution. An alternative approach is the use of state variables such as voltages and currents instead of field quantities where the FDTD algorithm is then operating in the framework of a corresponding passive equivalent circuit (EC). Such an EC representation is attractive because it bears a very intuitive access to the implementation of material dispersion. The first mention of EC FDTD appears, to our knowledge, in the publications of Gwarek *et al.* [3] and Craddock *et al.* [4]. Initial implementations of the proposed EC FDTD algorithm have been carried out for a regular Cartesian mesh, as it has been initially described in [5, 6] and more extensively in [7, 8]. Following Maxwell's equations, the proper EC formulation is directly deducible from its differential form (which is certainly constitutive for the conventional FDTD scheme) or from its integral form, where the latter defines the very starting point of our EC FDTD scheme as well as for other methods such as the well-established finite-integral technique (FIT) [9, 10]. In either case, the EC FDTD algorithm can easily be translated back and forth to the conventional FDTD formulation and therefore retains most of its advantages and disadvantages, concerning, for example, numerical accuracy and stability.

*Correspondence to: Thorsten Liebig, General and Theoretical Electrical Engineering (ATE), Faculty of Engineering, University of Duisburg-Essen, and CENIDE - Center for Nanointegration Duisburg-Essen, Bismarckstr. 81, D-47057 Duisburg, Germany.
†E-mail: thorsten.liebig@uni-due.de

It is worth noting that the EC FDTD formulation has clear benefits such as a reduced numerical effort inside the iteration loop because of a reduced number of multiplications (which is intrinsic to the representation with state variables such as voltages and currents) and the aforementioned intuitive incorporation of (highly) dispersive materials. For example, materials that are represented by multipolar Drude/Lorentz type models [7, 8] can be easily implemented along corresponding extensions of the associated EC in the form of small tailored filter sections, which mimics the material dispersion underlying, for example, plasmonic structures [11, 12], wide band-conducting sheet models [6], or even more challenging material properties such as biological tissue [13]. An additional virtue of the EC FDTD formulation is its affinity to an energy-based stability criterion [7, 8] that tends to be less strict than the usually applied Courant–Friedrich–Levy (CFL) stability criterion. Interestingly, this alternative criterion is in principle also applicable to the conventional FDTD scheme offering thus a promise for potentially larger time steps.

In the following, we will show that an adaption of our EC FDTD algorithm to a cylindrical mesh can be realized with only minimal changes to the EC FDTD operator coefficients allowing the use of a generic (and potentially highly optimized) EC FDTD iteration engine while enabling all well-known FDTD features (e.g., perfectly matched layer (PML) boundary conditions, Mur-absorbing boundary conditions, dispersive material models, and conducting sheet models) at virtually unaltered numerical efficiency. Please note that our cylindrical EC FDTD implementation is more general than the body of revolution version of FDTD provided, for example, by other FDTD simulation packages such as MEEP [14] because the body of revolution representation is restricted to rotationally symmetric problems, whereas our proposed method qualifies as a full vectorial three-dimensional (3D) EC FDTD scheme adapted to cylindrical r-coordinates, α-coordinates, and z-coordinates.

Cylindrical FDTD implementations—and in particular for magnetic resonance imaging (MRI) applications—have already been carried out, for example, by Trakic *et al.* [15] for the analysis of transient eddy currents stemming from switching magnetic field gradients as well as by Chi *et al.* [16] for the comprehensive analysis of radio-frequency (RF) field-tissue interactions. In addition, Wang *et al.* [17] proposed a parallelization scheme for an earlier FDTD version supporting both Cartesian and cylindrical meshes, which relies on a distributed memory architecture while adapting the message-passing interface (MPI) library. Chi *et al.* [16] was also offering a numerical regularization scheme for handling the polar-axis singularity apparent in the cylindrical implementation, using Ampère's and Faraday's laws as an indirect access to the field quantities in the singularity. Alternative measures based on corresponding coordinate transformations are proposed by Kancleris [18]. The authors [16] also speculates about the need for subgridding that may possibly become an issue to be considered because of the costly mesh refinement inherent to the morphology of the cylindrical discretization. In our paper, we will demonstrate that subgridding is less an option than an inevitable feature to be included in any cylindrical FDTD implementation because of the severe constraints posed by the CFL limit (or a similar energy-based criterion [7, 8]).

The remainder of the paper is organized as follows: after an introduction into the EC FDTD formulation for the Cartesian grid in Section 2, we will reiterate the EC FDTD formulation for the cylindrical Yee cell in Section 3 while investigating two emerging special cases of the staggered grid that only occur in a cylindrical mesh and, hence, how to handle these cases effectively. This also includes the regularization of the polar-axis singularity in the EC formulation following a similar approach as in [16]. In Section 4, we will address the issue of the reduced FDTD time step due to the mesh refinement present in any regular cylindrical grid and introduce an efficient subgridding strategy to counteract this unwanted numerical slow-down. The performance of the cylindrical EC FDTD implementation is presented in Section 5 along two examples, namely a simple benchmark problem and a showcase from our ongoing MRI research. In the framework of novel scanner schemes such as the high-field traveling wave (TW) MRI [19], where the RF magnetic field exposure is provided by propagating electromagnetic modes along the cylindrical MRI bore, we have analyzed thin ring antennas, on the basis of composite right/left-handed (CRLH) electromagnetic metamaterials [20] for molding the resulting wave fields [21, 22]. As these excitation antennas are conforming to the inner surface of the MRI bore, the resulting simulation problem becomes highly challenging because of the thin sophisticated features that are embedded in the large bore volume. We can show that the cylindrical EC FDTD

DOI: 10.1002/jnm

implementation turns out to be ideally suited to demonstrate the applicability of the metamaterial ring antennas as a holistic excitation and control scheme in traveling wave MRI.

Practical information regarding the proper implementation of the free and open source EC FDTD simulation platform openEMS [23] is provided in Section 6. This includes software issues as well as performance measures together with a short description of the user-friendly Matlab/Octave scripting interface. The interface is designed to setup, control, and evaluate the EC FDTD simulation and also acts as a simple graphical user interface (GUI) in the sense of a two-dimensional (2D)/3D structural viewer. Hence, openEMS is made available for public review, free use, and participative enhancement. A brief conclusion together with an outlook is finally drawn in Section 7.

2. THE EC FDTD FORMULATION IN CARTESIAN COORDINATES

The EC FDTD scheme in Cartesian coordinates is derived from Maxwell's equations in integral form,

$$\oint_{\partial\tilde{A}} \vec{H}\cdot\mathrm{d}\vec{s} = +\frac{\mathrm{d}}{\mathrm{d}t}\iint_{\tilde{A}} \varepsilon\vec{E}\cdot\mathrm{d}\vec{\tilde{A}} + \iint_{\tilde{A}} \kappa\vec{E}\cdot\mathrm{d}\vec{\tilde{A}} \tag{1}$$

$$\oint_{\partial A} \vec{E}\cdot\mathrm{d}\vec{s} = -\frac{\mathrm{d}}{\mathrm{d}t}\iint_{A} \mu\vec{H}\cdot\mathrm{d}\vec{A} - \iint_{A} \sigma\vec{H}\cdot\mathrm{d}\vec{A} \tag{2}$$

where all material properties, (permitivity ε, permeability μ, electric conductivity κ, and magnetic conductivity σ) are for clarity reasons considered nondispersive (i.e., frequency independent). These time-continuous and space-continuous equations have to be discretized using the well-known Yee cell [1] depicted in Figure 1.

The so-called primary grid (shown in red) is introduced by the user (or software) according to the given simulation structure. The electric field is defined on the edges originating on the primary node (N in Figure 1) of the primary grid, where the length of an edge, for example, in the x-direction, is labeled as Δ_x. It should be noted that the proposed scheme fully supports a graded mesh in any direction, which makes the length of the edges depend on the position inside the mesh. For a better readability, a notation such as $\Delta_\mathrm{x}(n_\mathrm{x})$ was omitted.

The faces of the primary Yee cell, for example, normal to the y-axis, are labeled A_y (cf. Figure 1(b)).

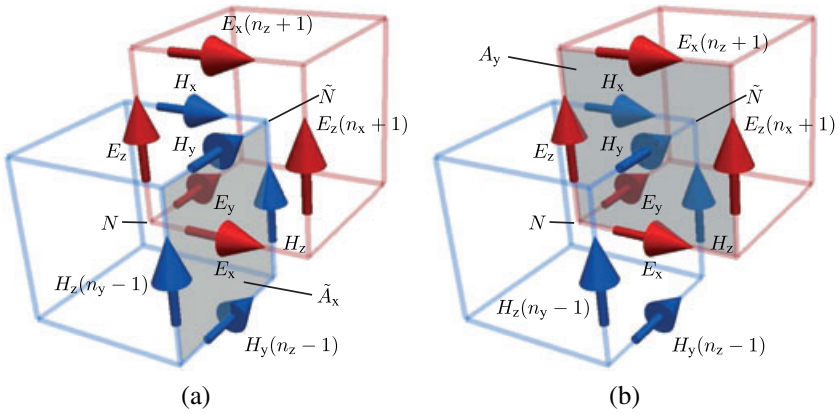

Figure 1. Yee cell (a) highlighting Ampère's law for the electric field in x-direction through surface $\tilde{A}_\mathrm{x}$ and in association with the surrounding magnetic field components in y-direction and z-direction and (b) highlighting Faraday's law for the magnetic field in y-direction through surface A_y and in association to the surrounding electric field components in x-direction and z-direction.

DOI: 10.1002/jnm

The vertices of the dual grid or dual Yee cell (depicted in blue) are located on the center points of the primary grid. All dual mesh parameters are labeled with a tilde. The magnetic field is defined on the edges of this dual mesh (pointing towards the node $\tilde{N}$).

Discretizing Ampère's law for the exemplarily chosen surface $\tilde{A}_\mathrm{x}$ from figure 1(a) yields

$$H_\mathrm{y}\Delta_\mathrm{y} - H_\mathrm{y}(n_\mathrm{z}-1)\Delta_\mathrm{y} - H_\mathrm{z}\Delta_\mathrm{z} + H_\mathrm{z}(n_\mathrm{y}-1)\Delta_\mathrm{z} \approx \tilde{A}_\mathrm{x}\left(\varepsilon\frac{\mathrm{d}}{\mathrm{d}t}E_\mathrm{x} + \kappa E_\mathrm{x}\right) \tag{3}$$

Discretizing Faraday's law, for example, for the surface A_y as highlighted in Figure 1(b), yields

$$E_\mathrm{z}\Delta_\mathrm{z} - E_\mathrm{z}(n_\mathrm{x}+1)\Delta_\mathrm{z} - E_\mathrm{x}\Delta_\mathrm{x} + E_\mathrm{x}(n_\mathrm{z}+1)\Delta_\mathrm{x} \approx -A_\mathrm{y}\left(\mu\frac{\mathrm{d}}{\mathrm{d}t}H_\mathrm{y} + \sigma H_\mathrm{y}\right) \tag{4}$$

Equations (3) and (4) are the well-known basis for the conventional FDTD method [1]. In the framework of EC FDTD, the basic quantities are neither electric nor magnetic fields. The EC FDTD algorithm rather relies on voltage and current state variables that are retrieved from the product of the corresponding field times the length of their associated edge derived as follows.

$$v_\mathrm{x} = E_\mathrm{x}\Delta_\mathrm{x}, \quad v_\mathrm{y} = E_\mathrm{y}\Delta_\mathrm{y}, \quad v_\mathrm{z} = E_\mathrm{z}\Delta_\mathrm{z} \tag{5a}$$

$$i_\mathrm{x} = H_\mathrm{x}\tilde{\Delta}_\mathrm{x}, \quad i_\mathrm{y} = H_\mathrm{y}\tilde{\Delta}_\mathrm{y}, \quad i_\mathrm{z} = H_\mathrm{z}\tilde{\Delta}_\mathrm{z} \tag{5b}$$

The physical unit of equation (5a) and (5b) is thus an edge voltage and edge current, respectively. Rewriting equation (3) while using this notation leads then to

$$i_\mathrm{y} - i_\mathrm{y}(n_\mathrm{z}-1) - i_\mathrm{z} + i_\mathrm{z}(n_\mathrm{y}-1) = C_\mathrm{x}\frac{\mathrm{d}}{\mathrm{d}t}v_\mathrm{x} + G_\mathrm{x}v_\mathrm{x} \tag{6}$$

$$\text{with} \qquad C_\mathrm{x} = \frac{\tilde{A}_\mathrm{x}\varepsilon}{\Delta_\mathrm{x}} \qquad \text{and} \qquad G_\mathrm{x} = \frac{\tilde{A}_\mathrm{x}\kappa}{\Delta_\mathrm{x}} \tag{7}$$

After rewriting equation (4), following the EC FDTD notation yields

$$v_\mathrm{z} - v_\mathrm{z}(n_\mathrm{x}+1) - v_\mathrm{x} + v_\mathrm{x}(n_\mathrm{z}+1) = -L_\mathrm{y}\frac{\mathrm{d}}{\mathrm{d}t}i_\mathrm{y} - R_\mathrm{y}i_\mathrm{y} \tag{8}$$

$$\text{with} \qquad L_\mathrm{y} = \frac{A_\mathrm{y}\mu}{\tilde{\Delta}_\mathrm{y}} \qquad \text{and} \qquad R_\mathrm{y} = \frac{A_\mathrm{y}\sigma}{\tilde{\Delta}_\mathrm{y}} \tag{9}$$

It should be noted at this point that equations (6) and (8) are still continuous in time. For the FDTD algorithm, the time dependency has to be discretized accordingly. Therefore, the voltages (electric fields) are sampled on the full time steps $n_\mathrm{t}\Delta_\mathrm{t}$, and the currents (magnetic fields) are sampled on each half time step $(n_\mathrm{t}+0.5)\Delta_\mathrm{t}$.

According to this, equation (6) can be evaluated at all half time steps, using a central difference for the voltage derivative:

$$C_\mathrm{x}\frac{v_\mathrm{x}^{n_\mathrm{t}} - v_\mathrm{x}^{n_\mathrm{t}-1}}{\Delta_\mathrm{t}} + G_\mathrm{x}\frac{v_\mathrm{x}^{n_\mathrm{t}} + v_\mathrm{x}^{n_\mathrm{t}-1}}{2} = i_\mathrm{y}^{n_\mathrm{t}-0.5} - i_\mathrm{y}^{n_\mathrm{t}-0.5}(n_\mathrm{z}-1) - i_\mathrm{z}^{n_\mathrm{t}-0.5} + i_\mathrm{z}^{n_\mathrm{t}-0.5}(n_\mathrm{y}-1) \tag{10}$$

DOI: 10.1002/jnm

Assuming that the voltages and currents prior to the current time step n_t are known, this yields the first update equation for, for example, the voltage v_x:

$$v_x^{n_t} = \frac{2C_x - \Delta_t G_x}{2C_x + \Delta_t G_x} v_x^{n_t-1} + \frac{2\Delta_t}{2C_x + \Delta_t G_x} \left(i_y^{n_t-0.5} - i_y^{n_t-0.5}(n_z - 1) - i_z^{n_t-0.5} + i_z^{n_t-0.5}(n_y - 1) \right) \tag{11}$$

In practice this means that no additional data have to be stored, and equation (11) will access the latest value of v_x that is of time step $n_t - 1$ and overwrite it to be the current voltage at time step n_t.

When the discretized time scheme is applied to equation (8), one obtains the expression:

$$L_y \frac{i_y^{n_t+0.5} - i_y^{n_t-0.5}}{\Delta_t} + R_y \frac{i_y^{n_t+0.5} + i_y^{n_t-0.5}}{2} = v_z^{n_t} - v_z^{n_t}(n_x + 1) - v_x^{n_t} + v_x^{n_t}(n_z + 1) \tag{12}$$

Again, given the voltages and currents prior to the time step $n_t + 0.5$, equation (12) yields the second update equation for, for example, the current i_y:

$$i_y^{n_t+0.5} = \frac{2L_y - \Delta_t R_y}{2L_y + \Delta_t R_y} i_y^{n_t-0.5} - \frac{2\Delta_t}{2L_x + \Delta_t R_y} \left(v_z^{n_t} - v_z^{n_t}(n_x + 1) - v_x^{n_t} + v_x^{n_t}(n_z + 1) \right) \tag{13}$$

The EC FDTD algorithm iteratively updates both sets of equations (11) and (13) until a particular termination criterion is met such as a complete dissipation of energy from the simulation domain or a steady state is reached in case of a sinusoidal excitation.

As mentioned in the introduction, the major advantage of the EC FDTD over the conventional FDTD method is its higher computational efficiency that can be recognized, for example, in voltage update equation (11). The EC FDTD needs only two coefficients and two multiplications for each update, compared with the three coefficients and multiplications for the conventional FDTD scheme. This overall reduction pays off with respect to a considerable speed and memory improvement of 33%.

It is worth mentioning that the EC FDTD bears some similarities to the so-called FIT [9], which can be viewed as a powerful extension of the FDTD scheme towards unstructured meshes. In FIT, four additional state variables are operational from the corresponding integral relations involving electric and magnetic flux densities as well as the current and charge densities. Referring to the smaller number of state variables, EC FDTD is believed to be numerically less expensive. It is although still supporting a high level of accuracy (compared with conventional FDTD) owing to the well-adapted sampling and averaging of material boundaries in the Yee cell that comes along with the EC form associated to the corresponding state variable.

3. THE EC FDTD FORMULATION IN CYLINDRICAL COORDINATES

The EC FDTD formulation for cylindrical coordinates is mostly identical to the Cartesian implementation as derived in Section 2. Figure 2 illustrates the Yee cell for the particular geometries. As for the Cartesian grid, Maxwell's equations (1) and (2) are evaluated on the surfaces and edges of the cylindrical Yee cell. The derivation of the final update/iteration equations is identical to the Cartesian case. The update equations for the two exemplary chosen voltage respective current state variable (cf. Figure 2) are therefore written as

$$v_r^{n_t} = \frac{2C_r - \Delta_t G_r}{2C_r + \Delta_t G_r} v_r^{n_t-1} + \frac{2\Delta_t}{2C_r \Delta_t G_r} \left(i_\alpha^{n_t-0.5} - i_\alpha^{n_t-0.5}(n_z - 1) - i_z^{n_t-0.5} + i_z^{n_t-0.5}(n_\alpha - 1) \right) \tag{14}$$

DOI: 10.1002/jnm

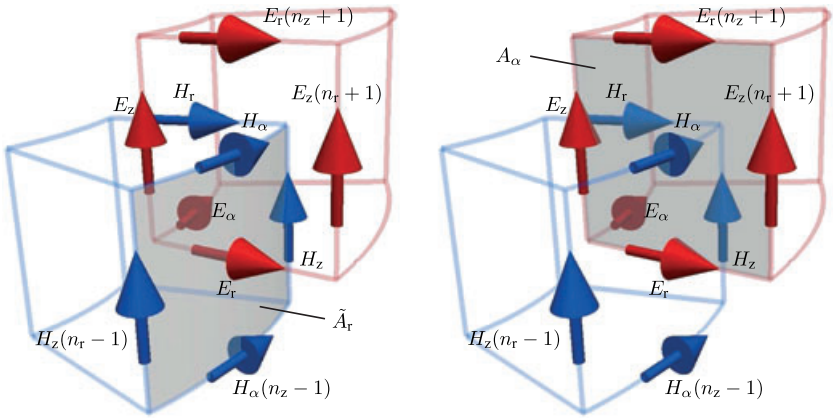

Figure 2. Yee cell (a) highlighting Ampère's law for the electric field in r-direction through surface $\tilde{A}_\mathrm{r}$ and in association to the surrounding magnetic field components in α-direction and z-direction and (b) highlighting Faraday's law for the magnetic field in α-direction through surface A_α and in association to the surrounding electric field components in r-direction and z-direction.

$$\text{with} \qquad C_\mathrm{r} = \frac{\tilde{A}_\mathrm{r}\varepsilon}{\Delta_\mathrm{r}} \qquad \text{and} \qquad G_\mathrm{r} = \frac{\tilde{A}_\mathrm{r}\kappa}{\Delta_\mathrm{r}} \tag{15}$$

$$i_\alpha^{n_\mathrm{t}+0.5} = \frac{2L_\alpha - \Delta_\mathrm{t}R_\alpha}{2L_\alpha + \Delta_\mathrm{t}R_\alpha} i_\alpha^{n_\mathrm{t}-0.5} - \frac{2\Delta_\mathrm{t}}{2L_\mathrm{r} + \Delta_\mathrm{t}R_\alpha}\left(v_\mathrm{z}^{n_\mathrm{t}} - v_\mathrm{z}^{n_\mathrm{t}}(n_\mathrm{r}+1) - v_\mathrm{r}^{n_\mathrm{t}} + v_\mathrm{r}^{n_\mathrm{t}}(n_\mathrm{z}+1)\right) \tag{16}$$

$$\text{with} \qquad L_\alpha = \frac{A_\alpha\mu}{\tilde{\Delta}_\alpha\tilde{r}} \qquad \text{and} \qquad R_\alpha = \frac{A_\alpha\sigma}{\tilde{\Delta}_\alpha\tilde{r}} \tag{17}$$

Comparing the EC FDTD update equations for the Cartesian mesh in equations (11) and (13) to the cylindrical mesh update equations (14) and (16) reveals the identical formulation for the update coefficients. The only difference between the Cartesian and cylindrical formulation emerges in the calculation of the surface areas A_d, $\tilde{A}_d$ (with $d \in \mathrm{r}, \alpha, \mathrm{z}$) and edge lengths Δ_d, $\tilde{\Delta}_d$ needed to evaluate the EC FDTD quantities C_d, G_d, L_d, and R_d. As well as for the Cartesian mesh, this formulation allows for an arbitrary mesh grading in r-direction, α-direction, or z-direction, if the appropriate mesh position is considered to calculate this quantities. Furthermore, it is important to note that the edge lengths in α-direction are a product of the respective angular widths Δ_α, $\tilde{\Delta}_\alpha$ and the edge radii r, $\tilde{r}$ (cf. equation (17)).

The mesh shown in Figure 3(a) is an example for a typical cylindrical mesh, but as distinguished from the Cartesian mesh, the cylindrical mesh encompasses two special cases that have to be handled

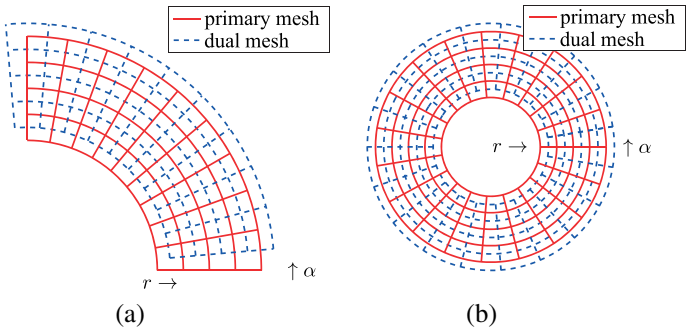

Figure 3. Yee cells of the staggered grid in a cylindrical coordinate system with (a) an "open" and with (b) a "closed" α-mesh.

DOI: 10.1002/jnm

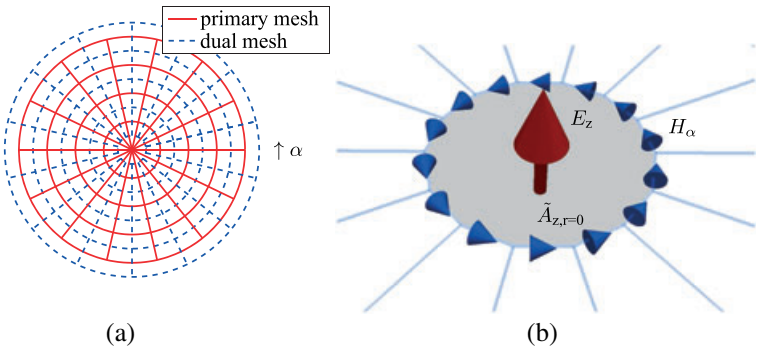

Figure 4. Yee cells in a cylindrical coordinate system encompassing the full angle of 360° and the $r = 0$ singular point. (a) gives a total view on the primary and dual mesh surrounding the cylindrical axis, and b) is demonstrating Ampère's law for determining the axis voltage $v_z^{n_1}(r = 0)$ in z-direction.

with care. The first one is a mesh that spans over the full angle of 360° (i.e., a "closed" α-mesh) as depicted in Figure 3(b). The second special case could be called a "full" cylindrical mesh, comprising a closed α-mesh and the mesh singularity at $r = 0$ (cf. Figure 4(a)). Both cases have to be handled by the EC FDTD algorithm:

3.1. Special case I: full 360° cylindrical mesh ("closed" α-mesh for r > 0)

Handling the first special case is quite simple and intuitive. Usually all field data are stored in a three-dimensional array, indexed in α-direction from $n_\alpha = 0$ to $n_\alpha = N_\alpha - 1$, with N_α the number of lines in α-direction.

To allow a round-trip propagation in the α-direction, the EC FDTD algorithm therefore must ensure that a voltage or current accessed at $n_\alpha = -1$ for the updating is properly mapped to $n_\alpha = N_\alpha - 1$ and vice versa.

Considering that the closed α-mesh would require an alteration of the usual EC FDTD update scheme, an alternative approach can be realized with introducing a (redundant) primary mesh line at both the angles $\alpha = 0$ and $\alpha = 2\pi$. In this case, the FDTD algorithm updates the tangential voltages for the last "alpha-line" and copies this data to the tangential voltages at the first alpha-line, which cannot be updated because of to the need of accessing a current value at $n_\alpha = -1$ (cf. equation (14)). Respectively, the currents for the first α-line can be updated and copied to the last current alpha-line.

Because openEMS can handle Cartesian and cylindrical coordinates within the same EC FDTD engine, the latter approach was chosen to allow usage of the optimized "conventional" iteration engine for both types of mesh, whereas only adding the described copy operations in case of a closed α cylindrical mesh situation as an engine extension (cf. Section 6).

3.2. Special case II: full cylindrical mesh (closed α-mesh bearing a singularity at r = 0)

The second special case that may occur in a cylindrical mesh is in fact a special case of the first special case and is depicted in Figure 4. It includes the 360° cylindrical mesh (cf. Section 3.1.) and the $r = 0$ singularity. For this singular point in the EC FDTD mesh, an extra EC FDTD operator has to be derived, but not all field components are affected: the magnetic field components (currents) that are located on the first dual mesh line with a radius larger than zero are unaffected. The electric field components (voltage v_r) in radial direction are located on the edge pointing away from $r = 0$ and are therefore not affected as well. All azimuthal electric field components (voltage v_α at $n_r = 0$) encompass this singular point, but because the α-direction is not defined for $r = 0$, the azimuthal component of the electric field remains undefined as well and can therefore be set to zero. The voltages associated to the electric field in z-direction are located at $r = 0$ as well, and Ampére's law has to be evaluated for this specific case. In [16], a similar approach was used for the conventional FDTD algorithm.

DOI: 10.1002/jnm

As visualized in Figure 4, the singular point is surrounded by dual mesh lines in α-direction. Therefore, Ampère's law can be used again to find an update equation for $v_z^{n_t}$ at the specific point $r = 0$. Evaluating equation (1) in a discretized manner for the surface $\tilde{A}_{z,r=0}$ as shown in Figure 4(b) yields

$$\sum_{n_\alpha=0}^{N_\alpha-1} H_\alpha \Delta_\alpha \tilde{r} = \tilde{A}_{z,r=0} \left(\varepsilon \frac{\mathrm{d}}{\mathrm{d}t} E_z + \kappa E_z \right) \tag{18}$$

A further discretization in the time domain yields an expression that can be rewritten as an EC FDTD update equations as follows:

$$v_z^{n_t}(r=0) = \frac{2C_{z,r=0} - \Delta_t G_{z,r=0}}{2C_{z,r=0} + \Delta_t G_{z,r=0}} v_{z,r=0}^{n_t-1} + \frac{2\Delta_t}{2C_{z,r=0} + \Delta_t G_{z,r=0}} \sum_{n_\alpha=0}^{N_\alpha-1} i_\alpha^{n_t-0.5} \tag{19}$$

$$\text{with} \qquad C_{z,r=0} = \frac{\varepsilon \tilde{A}_{z,r=0}}{\Delta_z} \qquad \text{and} \qquad G_{z,r=0} = \frac{\kappa \tilde{A}_{z,r=0}}{\Delta_z} \tag{20}$$

This additional update equation for the voltage $v_z^{n_t}(r = 0)$ along the cylindrical axis has to be evaluated after performing the conventional voltage updates (equations (14) and (16)).

3.3. Handling known FDTD features in cylindrical coordinates

There is a number of well-known and useful extensions added to the original FDTD algorithm over the last decades; of which, the most important ones are the absorbing boundary conditions to mimic, for example, free space surroundings for radiating structures. As shown in Section 3, the differences between the Cartesian and the cylindrical FDTD formulation merely occurs in the evaluation of the relevant geometrical measures within the Yee cell, namely the edge lengths, the surface areas, or the volume. Therefore, the implementation of additional FDTD features such as PML boundary conditions or dispersive material models into the cylindrical mesh is equally straightforward as for the standard Cartesian formulation. In the openEMS package (cf. Section 6), all these features have been included without special reference to the different mesh configurations because these extensions are all assignable to the generic EC FDTD iteration engine. Hence, the PML boundary conditions, dispersive material models, and so on work "out of the box" for both, Cartesian and cylindrical mesh, because the specific mesh characteristic is properly encapsulated in the openEMS implementation by using the C++ (object-oriented) inheritance concepts.

4. TIME STEP AND MULTIGRID APPROACH

In conventional FDTD schemes, the assignment of the maximal allowed time step is usually based on the CFL stability criterion [1], which in our case has been translated into the framework of EC FDTD [8, 11]. Although derived for the Cartesian mesh, numerous practical examples have proven the latter to be applicable to the cylindrical mesh as well. A rigorous stability proof for the cylindrical EC FDTD scheme is currently investigated and will be published elsewhere.

The largest possible time steps are highly desirable because they allow for less iterations and hence a faster simulation. Following the aforementioned stability criteria, the maximal time step is predefined by the dimensions of the smallest Yee cell. In a homogeneous Cartesian mesh, all cells are supposed to have the same size, whereas in a cylindrical mesh, the cell size is inevitably depending on the radial position of each cell (cf. Figures 4(a) and 6(b)). The mesh resolution in the azimuthal α-direction is

DOI: 10.1002/jnm

therefore chosen to have an acceptable cell size with respect to the outermost cells in the radial direction. This results in very thin cells for smaller radii and therefore in an unhandy small time step, where the latter may become the major drawback of a cylindrical EC FDTD implementation in comparison with its Cartesian counterpart. A possible solution to this problem is the use of a new multigrid approach for the cylindrical EC FDTD. Whereas for conventional (i.e., Cartesian) FDTD schemes, the multigrid approach is commonly adopted for achieving a local enhancement in the mesh resolution (and therefore the possible accuracy), the situation is reversed for the cylindrical mesh, where the subgrid is used to reduce the exaggerated resolution along the radial direction towards the origin. Figure 5 illustrates a full cylindrical mesh together with the subgrid for increasing the cell size around the origin. The enlarged subgrid was setup while omitting every second radial line of the primary mesh yielding an increase of the relevant cell size by a factor of two and hence a correspondingly increased time step.

For large computational domains, the multigrid approach can be nested several times. The example shown in Figure 6(a) employs a three-staged subgrid to keep the average cell size as uniform as possible (cf. the regular grid in Figure 6(b)) resulting in an increase of the time step by a factor of $2^3 = 8$. The corresponding speedup even outperforms this factor of 8 because of the reduced overall number of Yee cells. To benefit from all these speedup contributions, a careful design of the multistaged subgrids is still mandatory because subgridding is only effective if the smallest grid size is enlarged accordingly, while coarsening the mesh resolution towards the origin. For example, this means that any additional subgrid to the mesh shown in Figure 6(a) would only slightly (or not at all) increase the time step, given that the smallest cell is already located in the original mesh instead in any of the subsequent subgrids. When following such reasoning, we obtain a twofold interrelated meshing condition, first with respect to the uniformity of the average cell size and second a limit for the recommendable number of stages in the nested subgrids.

An important issue of the multigrid approach is an emergent numerical overhead stemming from necessary field transfers and interpolations at the interfaces between the different (sub)grids. In case of the electric field strengths (i.e., edge voltages) this is quite intuitive. The fields in z-direction are located at the same positions and just need to be copied between the different engines. In the α-direction two adjacent edge voltages can be added to obtain the edge voltage in the coarser subgrid. Looking at the

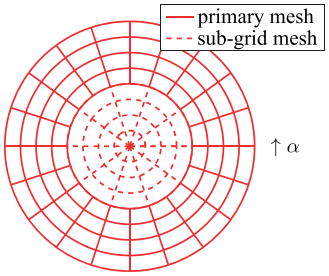

Figure 5. Primary mesh in a cylindrical coordinate system with a subgrid around the singular point in the center.

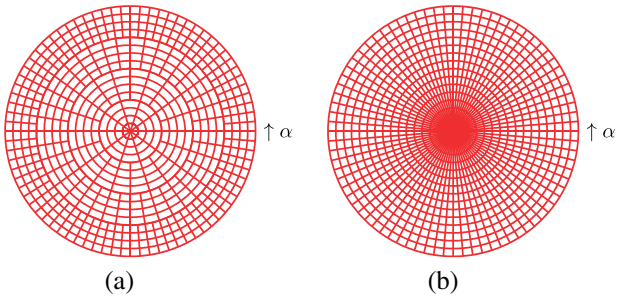

Figure 6. Comparison of a mesh in a cylindrical coordinate system with three nested subgrids (a) and the original mesh without any subgrid (b).

DOI: 10.1002/jnm

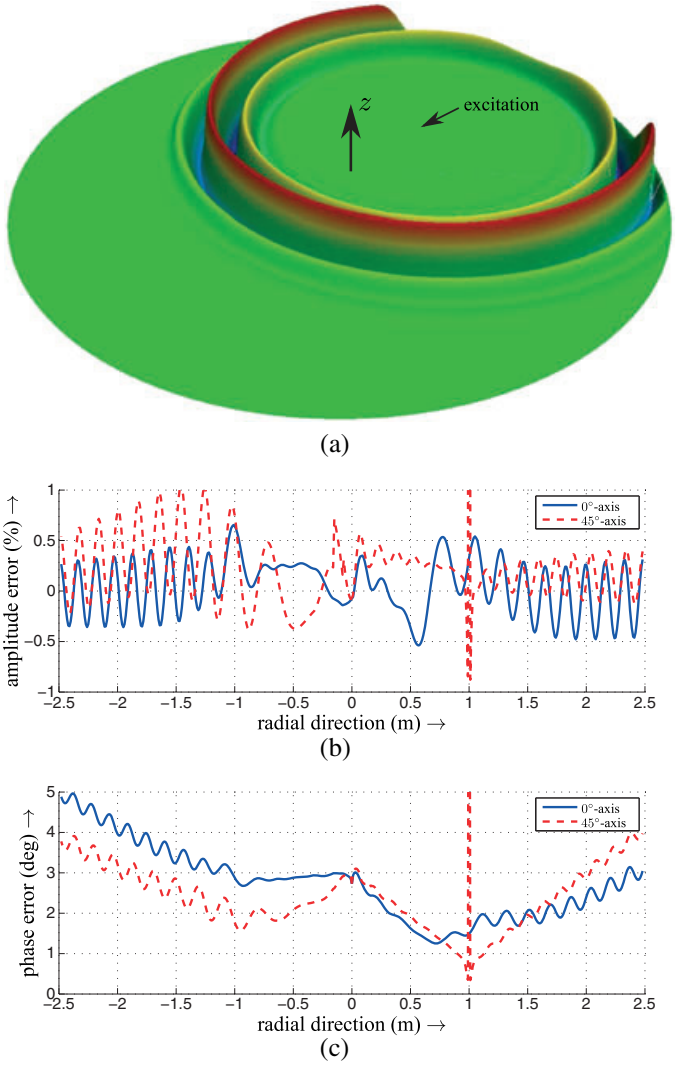

Figure 7. Numerical benchmark example showing an evolving two-dimensional cylindrical wave packet (E_z, H_x, H_y) on a cylindrical mesh with an "off-center" Gaussian-pulse excitation at $r = 1$ m and $\alpha = 45°$. The circular simulation domain has a radius of 2.5 m and is discretized along 256 mesh lines in radial direction and 1600 mesh lines in azimuthal direction, where the truncation of the domain is realized with a perfectly matched layer boundary. Five nested subgrids were used to reduce the simulation time by a factor of ∼32. The plots display (a) the E_z component for a certain time step, (b) the amplitude error, and (c) the phase error, both along the x-axis (0°-axis) and 45°-axis. The errors are derived from the comparison to an analytical two-dimensional cylindrical wave at a frequency of 1 GHz.

magnetic field components (i.e., edge currents) in the staggered grid, things become more complicated because the edge currents are defined at different locations with respect to the angular direction. In the current implementation, a linear interpolation is used to compute the edge currents for the finer primary grid. From observations, this simple interpolation scheme has proven stable during all previous numerical experiments, although a rigorous stability analysis is still advisable. It is worth mentioning that the additional computing effort for each time step is by far counterbalanced by the speedup resulting from the reduced number of Yee cells in the subgrids.

Figure 7 displays a benchmark example showing a 2D cylindrical wave (E_z, H_x, H_y) excited "off-center" within a correspondingly meshed cylindrical domain with a radius of 2.5 m.[†]

[†]Download example at http://openems.de/index.php/Tutorial:_2D_Cylindrical_Wave

DOI: 10.1002/jnm

When supporting an excitation bandwidth, for example, within the spectral range of 0–2 GHz, the mesh resolution has to be chosen accordingly—namely with respect to the outmost boundary of the cylindrical domain—leading to 1600 azimuthal mesh lines. This outmost boundary is actually represented by a PML for the truncation of the overall simulation domain in the radial direction. To study the scaling behavior, five subgrid stages were introduced where the resulting numerical performance is then compared with the initial one on the basis of the full cylindrical mesh. An increase in the time step by a factor of 31.94 was deduced from simulations, which is obviously very close to the theoretically achievable maximum of $2^5 = 32$ rendering our FDTD scheme very efficient.

For further validation, we compared the 1 GHz spectral component of an evolving wave packet with the analytical representation of a corresponding 2D cylindrical wave train. A very good agreement can be deduced from Figure 7(b)–(c)), yielding an amplitude error (cf. Figure 7(b)) that is below 1% within the entire simulation domain (except at the singular excitation point). The phase error (cf. Figure 7(c)) is very small as well, especially when considering that this error is still below 5° at the furthest domain boundary where the wave has already traveled a distance of several wavelengths ($\lambda \approx 0.3$ m). As the error figures also contain contributions owing to numerical dispersion, one can conclude that our multiple subgridding strategy is perfectly apt to retain the accuracy needed in highly efficient 3D computational electromagnetics analysis.

5. A SHOWCASE IN HIGH-FIELD (7T) MAGNETIC RESONANCE IMAGING

The development of the cylindrical EC FDTD algorithm has been mainly motivated by our ongoing research in the realm of high-field MRI [21,22]. Many devices used in this particular context confine to a cylindrical shape, such as the bore of the MRI scanner and the birdcage coils, where the latter has to conform to the cylindrical geometry within the scanner because of spatial constraints. The RF coils play an essential part in the resonant excitation of the nuclei at their corresponding Larmor frequency. The MRI bore is surrounded by a conducting RF shield to provide a decoupling between the RF system and the gradient coils, which are responsible for addressing the spatial information in the analyzed tissue volume. From a distinct RF viewpoint, the MRI scanner simply boils down to a large cylindrical metal shield having a typical diameter of 64 cm and a length around 3 m. This shield encloses the patient's body, where the magnetic RF field is delivered and received inside the shield by using the aforementioned resonant coils or antenna structures. In numerical terms, the RF system of the MRI scanner defines a highly challenging problem, given that the large cylindrical volume may usually host structures of very small and thin feature sizes. The RF aspect of the MRI scanner system is pronounced even further in the framework of a novel approach that has been recently presented by Brunner *et al.* [19]. Here, the RF magnetic field is distributed by a circularly polarized traveling TE_{11} wave while exploiting the bore's RF shield in the very sense of a circular waveguide. To mold this traveling wave field accordingly, we have proposed (following our statement in [22]) "an adaptive RF antenna system consisting of multiple 'flat' CRLH metamaterial ring antennas that fully conform to the inner surface of the MRI bore, and hence yields no drawback in terms of patient's comfort" (cf. Figure 8).

A proper choice for the numerical analysis of such traveling wave MRI scenario would preferably rely on an unstructured mesh that underlies, for example, the finite-element method, to handle the "small" conformal structures. When addressing the around one cubic meter of space inside the MRI bore together with the tiny features of a conformal CRLH antenna, finite-element method is ruled out because of the exceeding computational costs. In contrast, direct solvers as the FDTD method are known to be highly memory efficient for extensive simulation domains and resolutions because the computational costs scale linearly with the number of cells.

Figure 8 depicts the traveling wave MRI model for the cylindrical EC FDTD simulation, where the MRI bore is populated with an equidistant arrangement of 15 conformal CRLH ring antennas. Each ring antenna consists of 32 periodic substructures (i.e., unit cells) implemented by two metal layers, which extends on both sides of a printed circuit board (PCB) substrate with a thickness of 1.28 mm (cf. inset of Figure 8). The PCB rings are then placed 10 mm apart from the ground layer represented by the cylindrical RF shield. The suitability of the graded cylindrical meshing is displayed in Figure 9

DOI: 10.1002/jnm

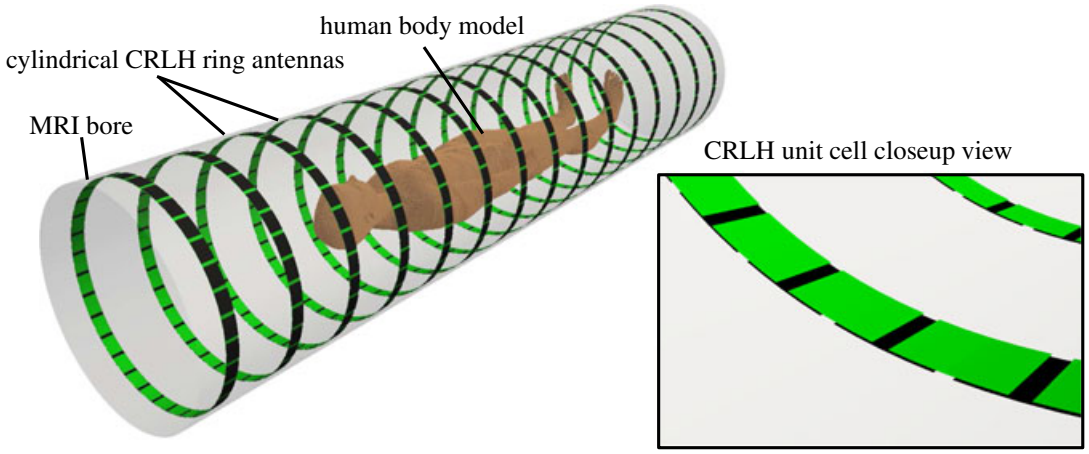

Figure 8. OpenEMS model of a magnetic resonance imaging (MRI) bore with a 64 cm diameter and a total length of 3 m, cladded with composite right/left-handed (CRLH) ring antennas and containing the human phantom model of the Virtual Family [24]. The common ground is represented by the cylindrical radio-frequency shield behind the bore (not shown).

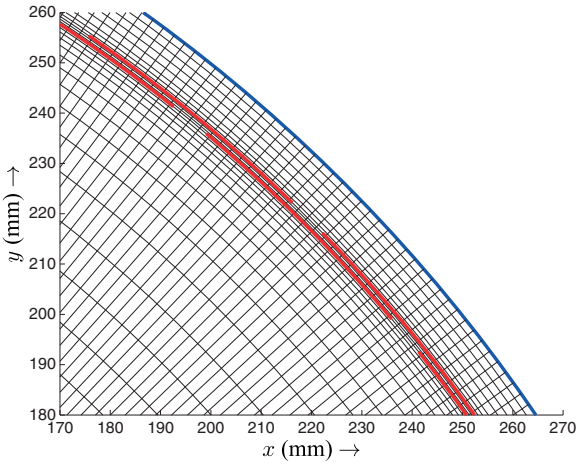

Figure 9. Inhomogeneous cylindrical mesh used to discretize the unit cells of the composite right/left-handed ring antennas. It consists of 768 lines in α-direction and 58 lines in radial direction. The thin metal layers are highlighted.

showing a detailed view of the conformal CRLH ring antenna. The thin PCB substrate has been omitted for clarity reasons to expose how nicely the mesh conforms with the thin features of the antenna's unit cell. For achieving a comparable numerical accuracy with a Cartesian mesh, the resolution would have to be significantly enhanced to minimize the influence of the stair casing. This would require up to 100 times more Yee cells to resolve the curved multilayer structure and hence a significantly decreased time step. In terms of memory consumption and simulation time, a conventional FDTD scheme would barely be capable to handle the posed MRI problem.

With the cylindrical EC FDTD implementation in openEMS, the overall MRI setup can be evaluated even with a surrounding air buffer to account for the influence of the fringe fields (i.e., the associated wave reflections) at both open bore ends. The CRLH ring antennas (cf. Figure 8) are designed in such a way that they mimic the TE_{11} mode's current distribution at the corresponding location in the cylindrical wall, yielding an effective excitation of TE_{11} traveling waves in both positive and negative z-direction. By optimizing the RF excitation amplitudes and phases in each of the 15 ring antennas, we have shown [21, 22] that virtually any desired H-field profile along the z-direction could be achieved. A typical example is given in Figure 10 where a set of excitations was tailored that way to obtain a

DOI: 10.1002/jnm

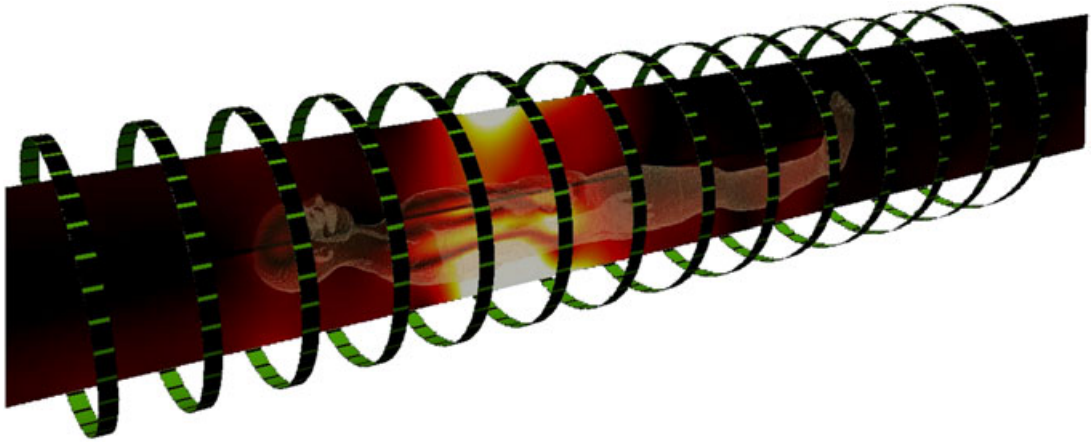

Figure 10. Magnetic field strength $\left(\sqrt{H_r^2 + H_\alpha^2 + H_z^2}\right)$ distribution optimized for a uniform local field window around the abdomen and a reduced field strength for all other body parts—especially the head—to reduce the specific absorption rate.

traveling RF magnetic field within a confined window to obtain a preferably uniform illumination of the patient's abdomen.

Especially when looking at complex electromagnetic optimization scenarios, high-speed full-wave time-domain methods with conformal meshing such as the proposed cylindrical EC FDTD implementation will become an indispensable tool for designing advanced RF systems not only in the realm of MRI or biomedical engineering.

6. THE openEMS PACKAGE

Both the Cartesian and cylindrical EC FDTD algorithms (cf. Sections 2 and 3) with all its special features are incorporated in our free and open source simulation platform openEMS. The fast and highly optimized EC FDTD operator and the EC FDTD engine have been implemented utilizing an extensive C++ class concept that efficiently encapsulates the conceptual differences in the mesh types currently supported by openEMS. Thereby, the generic EC FDTD engine was kept as simple as possible to maximize computation efficiency while using multithreading, the SSE processor instruction sets, and a compressed FDTD operator to allow for high-speed simulations (e.g., >150 MC/s on an Intel Core-i7 920 processor). Additionally, openEMS supports the MPI to distribute simulation tasks on a computer cluster (or supercomputer) aiming at even faster simulations of huge computational domains. In our laboratory, we performed simulation benchmarks with about 400 Million Yee cells (2.4 billion unknowns) on our Linux cluster with 15 off-the-shelf PCs yielding an aggregate simulation speed of >2 GC/s (two billion cells per second).

Furthermore, a modern engine extension framework was introduced in openEMS to incorporate, for example, advanced material models. This means that the capability of a conventional EC FDTD engine can be significantly enhanced by a virtually unlimited number of engine extensions for the realization of, for example, highly specific FDTD features. Each extension in the EC implementation is allowed a controlled access to the edge voltages and edge currents prior and after each update cycle of the main engine to fulfill their dedicated tasks. Currently, openEMS supports the following engine extensions: Mur and UPML boundary conditions [1], multipolar Drude material models [7, 8], and a conducting sheet model [6]. The engine extension framework is also adopted for the implementation of the proper field excitation, the special handling of different mesh types (i.e., the cylindrical mesh), and the MPI interface transfers to efficiently manage the corresponding domain decomposition. The advantage of this extension concept is a highly generic, fast, reliable, and easy-to-maintain (EC)-FDTD "core" engine without need to surrender its manageability to any additional feature that may be desirable in a specific application. A minor deceleration mechanism inherent to this approach owes to the additional access to the field data. This access (which is unavoidable in any case) would be less time consuming if directly incorporated into the FDTD engine itself but has to be implemented

DOI: 10.1002/jnm

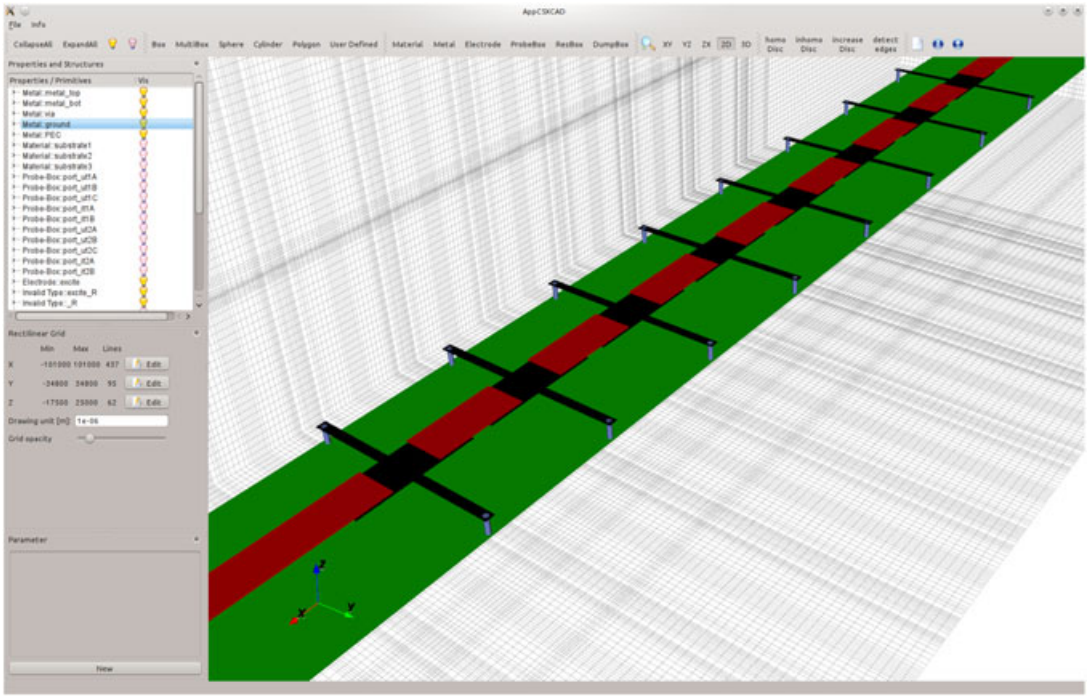

Figure 11. Three-dimensional view in the graphical user interface for openEMS (AppCSXCAD) showing a composite right/left-handed leaky wave antenna with eight unit cells. This tutorial example is available at `http://openEMS.de`.

at the expense of the intended modularity. Currently, the benefits of the generic engine outweigh this disadvantage. For future implementations, a combined approach may become feasible if often-used extensions (e.g., the UPML) are incorporated into the generic engines, whereas keeping other features as optional engine extension.

In the current implementation, OpenEMS does not rely on a highly sophisticated GUI to setup and visualize FDTD simulation tasks as provided by most of the commercially available FDTD software packages. Instead, openEMS comes with an easy-to-use Matlab interface, where even complex structures are efficiently setup employing the Matlab scripting language. In addition, the user can gain access to all field components produced by openEMS, which allows for a high flexibility especially with respect to further postprocessing such as visualization. Hence, a simple GUI is made available to visualize and review the structure in a 2D or 3D view (cf. example in Figure 11).

The Matlab interface allows to perform extensive numerical (structural) optimizations, for example, by using tailored smart search heuristics or the optimization toolbox provided by Matlab. As an alternative to Matlab, the free and open source platform GNU Octave[‡]) is also recommended.

We hope to encourage and create a community who contributes new features, extensions, and enhancements to openEMS. Some of these improvements could be provided by, for example, scrutinizing or extending the documentation, creating new tutorial examples or new (dispersive) material models. Further contributions could be, for example, an enhanced and automated mesh generator or combining openEMS with other (free) software projects, such as a circuit designer (e.g., Agilent ADS[§] or Qucs[¶]).

The complete source code, the corresponding binaries, and the installation instructions (Linux and Windows) together with a comprehensive documentation as well with a growing collection of tutorial examples are made available at `http://openEMS.de`.

[‡]GNU Octave: http://www.gnu.org/software/octave/
[§]Advanced Design System (ADS): www.agilent.com/find/eesof-ads
[¶]Quite Universal Circuit Simulator: http://qucs.sourceforge.net/

DOI: 10.1002/jnm

7. CONCLUSIONS AND OUTLOOK

We have presented an EC FDTD algorithm initially for the conventional Cartesian mesh and demonstrated the high affinity of this EC FDTD formulation to a cylindrical mesh implementation, where the latter just boils down to a different computation of the mesh specific edge lengths and cell areas. Thus, the very efficient and straightforward implementation of a generic EC FDTD engine has become possible, which supports both types of meshes and was made available within our free and open source simulation platform openEMS. Two special cases of the full cylindrical mesh (namely a 360° cylindrical mesh with and without the $r = 0$ singularity) have been discussed while providing solutions to both the azimuthal round-trip wave propagation and the appropriate handling of the polar-axis singularity by using a particularly tailored EC FDTD operator. To address the time-stepping issue that goes along with the decrease in cell size when progressing towards the polar-axis singularity, we showed that it is mandatory to choose appropriate subgridding schemes to keep up with a practical simulation speed. Hence, the consistent use of cascaded subgrids within the cylindrical mesh enables the user to maintain large enough time steps so that the simulation speed remains virtually unaffected by the evolution of the cell sizes in the neighborhood of the $r = 0$ singularity. Compared with the cumbersome computation within a conventional cylindrical mesh, our new subgridding strategy (i.e., the piecewise decrement of the azimuthal grid resolution while approaching the singularity) was capable to provide a speedup by a factor of 2 for each cascaded subgrid. One of our main motivations for the development of an efficient cylindrical EC FDTD has been addressed in Section 5 in conjunction with our current MRI research. Within a simulation showcase that is ideally suited to highlight the advantage of inhomogeneous cylindrical meshing, we analyzed a very flexible traveling wave excitation scheme consisting of multiple conformal metamaterial ring antennas. These "flat" ring antennas were mounted on the inner bore surface of a high-field (7T) MRI scanner, defining highly sophisticated features within the large bore volume. The huge size contrasts inherent to this structure are only tractable with a FDTD scheme that supports cylindrical meshing in conjunction with multiple cascaded subgrids. In this regard, the openEMS platform is unique compared with other FDTD packages such as MEEP [14] and virtually all of the commercial solvers. Especially the capabilities to create a simple structural sweep using the openEMS Matlab interface greatly supports the optimization and evaluation of the envisioned "MetaBore" concepts presented in [21, 22]. The inclusion of highly specific material models with complex dispersion relations is straightforward because they just confine to corresponding extensions assigned to the generic FDTD engine. Owing to the flexibility provided by openEMS, the meshing and material descriptions are easily adaptable to conform applications much different than our case study, namely biological tissue and composite modeling (bioelectromagnetics), optical antennas and plasmonics (nanophotonics), and multiwalled nanotubes and nanotransmission lines (nanoelectromagnetics). The openEMS platform is now ready for use and—above all—open to the community to contribute many additional and exciting new engine extensions making openEMS a valuable collective venture that hopefully becomes beneficial to all dedicated users.

REFERENCES

1. Taflove A, Hagness S. *Computational Electrodynamics: The Finite-difference Time-domain Method*, 3rd edn. Artech House: Norwood, MA, 2005.
2. Kunz K. *The Finite Difference Time Domain Method for Electromagnetics*. CRC Press: Boca Raton, USA, 1993.
3. Gwarek WK. Analysis of an arbitrarily-shaped planar circuit – a time-domain approach. *IEEE Transactions Microwave Theory and Techniques* 1985; **MTT-33**(10):1067–1072.
4. Craddock IJ, Railton CJ, McGeehan JP. Derivation and application of a passive equivalent circuit for the finite difference time domain algorithm. *IEEE Microwave and Guided Wave Letters* 1996; **6**(1):40–42.
5. Lauer A, Wolff I. Stable and efficient ABCs for graded mesh FDTD simulations, *IEEE MTT-S International Microwave Symposium Digest,* Vol. 2, Baltimore, MD, 1998; 461–464.
6. Lauer A, Wolff I. A conducting sheet model for efficient wide band FDTD analysis of planar waveguides and circuits, *IEEE MTT-S International Microwave Symposium Digest,* Vol. 4, Anaheim, CA, 1999; 1589–1592, DOI: 10.1109/MWSYM.1999.780262.
7. Rennings A, Lauer A, Caloz C, Wolf I. *Equivalent Circuit (EC) FDTD Method for Dispersive Materials: Derivation, Stability Criteria and Application Examples*, Springer Proceedings in Physics, vol. 121. Springer-Verlag: Berlin, 2008; 211–238.
8. Rennings A. Elektromagnetische zeitbereichssimulationen innovativer antennen auf basis von metamaterialien. *PhD Thesis*,

University of Duisburg-Essen, September 2008.
9. Weiland T. Time domain electromagnetic field computation with finite difference methods. *International Journal of Numerical Modelling: Electronic Networks, Devices and Fields* July 1996; **9**(4):295–319.
10. van Rienen U. *Numerical Methods in Computational Electrodynamics – Linear Systems and Practical Applications*. Springer: Berlin, 2001.
11. Rennings A, Mosig J, Caloz C, Erni D, Waldow P. Equivalent circuit (EC) FDTD method for the modeling of surface Plasmon based couplers. *Journal of Computational and Theoretical Nanoscience* April 2008; **5**(4): 690–703.
12. Rennings A, Mosig J, Gupta S, Caloz C, Kashyap R, Erni D, Waldow P. Ultra-compact power splitter based on coupled surface Plasmons, *International Symposium on Signals, Systems and Electronics, 2007. ISSSE '07*, Montréal, Québec, Canada, 2007; 471–474. DOI: 10.1109/ISSSE.2007.4294515.
13. Huclova S, Erni D, Fröhlich J. Modelling effective dielectric properties of materials containing diverse types of biological cells. *Journal of Physics D: Applied Physics* September 2010; **43**(36):365 405–1–10.
14. Oskooi AF, Roundy D, Ibanescu M, Bermel P, Joannopoulos JD, Johnson SG. MEEP: a flexible free-software package for electromagnetic simulations by the FDTD method. *Computer Physics Communications* January 2010; **181**:687–702. DOI: 10.1016/j.cpc.2009.11.008.
15. Trakic A, Wang H, Liu F, Lopez HS, Crozier S. Analysis of transient Eddy currents in MRI using a cylindrical FDTD method. *Applied Superconductivity, IEEE Transactions on* September 2006; **16**(3): 1924–1936. DOI: 10.1109/TASC.2006.874000.
16. Chi J, Liu F, Xia L, Shao T, Crozier S. An improved cylindrical FDTD algorithm and its application to field-tissue interaction study in MRI. *IEEE Transactions on Magnetics* February 2011; **47**(2):466–470. DOI: 10.1109/TMAG.2010.100098.
17. Wang H, Trakic A, Xia L, Liu F, Crozier S. An MRI-dedicated parallel FDTD scheme. *Concepts in Magnetic Resonance Part B: Magnetic Resonance Engineering* 2007; **31B**(3):147–161. DOI: 10.1002/cmr.b.20092.
18. Kancleris Z. Handling of singularity in finite-difference time-domain procedure for solving Maxwell's equations in cylindrical coordinate system. *IEEE Transactions on Antennas and Propagation* February 2008; **56**(2):610–613, DOI 10.1109/TAP.2007.915478.
19. Brunner DO, Zanche ND, Fröhlich J, Paska J, Pruessmann KP. Travelling-wave nuclear magnetic resonance. *Nature* February 2009; **457**:994–998.
20. Caloz C, Itoh T. *Electromagnetic Metamaterials: Transmission Line Theory and Microwave Applications: The Engineering Approach*. Wiley-Interscience: New York, 2006.
21. Erni D, Liebig T, Rennings A, Koster NHL, Fröhlich J. Highly adaptive RF excitation scheme based on conformal resonant CRLH metamaterial ring antennas for 7-Tesla traveling-wave magnetic resonance imaging, *33th Annual International Conference of the IEEE Engineering in Medicine and Biology Society (IEEE EMBS 2011)*, Bosten, MA, USA, 2011; 554–558.
22. Liebig T, Erni D, Rennings A, Koster NHL, Fröhlich J. MetaBore - a fully adaptive RF field control scheme based on conformal metamaterial ring antennas for high-field traveling-wave MRI. *Magnetic Resonance in Physics, Biology and Medecine (MAGMA)*; **24**:37–38. Special Supplement on the European Society for Magnetic Resonance in Medicine and Biology 28th Annual Science Meeting (ESMRMB 2011), paper 49 (talk and poster), pp. 22, October 6-8, Leipzig, Germany, 2011.
23. Liebig T. *openEMS - Open Electromagnetic Field Solver*. Available at: http://openEMS.de. [Accessed on: 10/07/2012].
24. Christ A, Kainz W, Hahn EG, Honegger K, Zefferer M, Neufeld E, Rascher W, Janka R, Bautz W, Chen J, *et al.* The Virtual Family – development of surface-based anatomical models of two adults and two children for dosimetric simulations. *Physics in Medicine and Biology* January 2010; **55**: N23–N38. DOI: 10.1088/0031-9155/55/2/N01.

AUTHORS' BIOGRAPHIES:

Thorsten Liebig received his diploma degree in electrical engineering from the University of Duisburg Essen in 2007. Since October 2007, he is a PhD student at the Laboratory for General and Theoretical Electrical Engineering at the University of Duisburg-Essen, Germany (http://www.ate.uni-due.de/). His current research includes applied electromagnetics and electromagnetic metamaterials for applications in MRI imaging, as well as numerical methods for computational electromagnetics. He is a creator and main developer of the free and open-source equivalent-circuit FDTD simulation platform openEMS (http://openEMS.de/).

Andreas Rennings studied electrical engineering at the University of Duisburg-Essen, Germany. He carried out his diploma work at the Microwave Electronics Laboratory of the University of California at Los Angeles. He received his Dipl.-Ing. and Dr.-Ing. degrees from the University of Duisburg-Essen in 2000 and 2008, respectively. From 2006 to 2008, he was with IMST GmbH in Kamp-Lintfort, Germany, where he worked as an RF engineer. Since then, he is a senior scientist at the Laboratory for General and Theoretical Electrical Engineering of the University of Duisburg-Essen, where he is a project leader in the field of bioelectromagnetics and med-tech. His general research interests include all aspects of theoretical and applied electromagnetics, currently with a focus on medical applications. He has authored and co-authored over 60 conference and journal papers and one book chapter and filed eight patents. He received several awards, including the second price within the student paper competition of the 2005 IEEE Antennas and Propagation Society International Symposium and the VDE-Promotionspreis 2009 for his doctoral thesis.

Sebastian Held studied electrical engineering at the University of Duisburg-Essen, Germany. He carried out his diploma work at the Institute of Microwave and RF Technology and received his Dipl.-Ing. degree in 2004. There he worked until 2009 as a research assistant in the field of antennas and RF circuit design. In 2009, he joined the Laboratory for General and Theoretical Electrical Engineering where he was involved in the development of active electromagnetic metamaterial antennas for automotive applications. Since 2011, he is with SIM Scientific Instruments Manufacturer GmbH at Oberhausen, Germany, where he works as a hardware and software engineer.

Daniel Erni received his diploma degrees from the University of Applied Sciences in Rapperswil in 1986 and from ETH Zürich in 1990, both in electrical engineering. Since 1990, he has been working at the Laboratory for Electromagnetic Fields and Microwave Electronics, ETH Zürich, where he obtained his PhD degree in 1996. From 1995-2006, he has been the founder and head of the Communication Photonics Group at ETH Zürich. Since October 2006, he is a full professor for General and Theoretical Electrical Engineering at the University of Duisburg-Essen, Germany (http://www.ate.uni-due.de/). His current research includes advanced data transmission schemes (i.e., O-MIMO) in board-level optical interconnects, optical on-chip interconnects, ultra-dense integrated optics, nanophotonics, plasmonics, quantum optics, electromagnetic and optical metamaterials, and applied electromagnetics (cf. electromagnetic metamaterials for applications in MRI imaging). On the system level, he has pioneered the introduction of numerical structural optimization into dense integrated optics device design. Further research interests include science and technology studies as well as the history and philosophy of science with a distinct focus on the epistemology in engineering sciences. He is a member of the editorial board of the *Journal of Computational and Theoretical Nanoscience* and edited the 2009 Special Issue on *Functional Nanophotonics and Nanoelectromagnetics*. He is a fellow of the Electromagnetics Academy, a member of the Center for Nanointegration Duisburg-Essen, and an associated member of the Swiss Electromagnetics Research Centre, as well as a member of the Swiss Physical Society, the German Physical Society, the Optical Society of America, and the IEEE.

DOI: 10.1002/jnm